Conjugate and bending faults drive the multiplex ruptures during the 2014 Mw 6.2 Thailand earthquake

Tira Tadapansawut[1,*], Yuji Yagi[2], Ryo Okuwaki[2,3,4], Shinji Yamashita[5], & Kousuke Shimizu[5]

[1] Graduate School of Life and Environmental Sciences, University of Tsukuba, Tsukuba, Ibaraki 305-8572, Japan.

[2] Faculty of Life and Environmental Sciences, University of Tsukuba, Tsukuba, Ibaraki 305-8572, Japan

[3] Mountain Science Center, University of Tsukuba, Tsukuba, Ibaraki 305-8572, Japan.

[4] COMET, School of Earth and Environment, University of Leeds LS2 9JT, UK.

[5] Graduate School of Science and Technology, University of Tsukuba, Tsukuba, Ibaraki 305-8572, Japan

[*] Corresponding author: Tira Tadapansawut (tira.tadapansawut@gmail.com)

ABSTRACT

A moment magnitude 6.2 crustal earthquake occurred in northern Thailand on 5 May 2014, and its aftershocks exhibit several lineaments with conjugate pattern, involving geometric complexity in a multi-segmented fault system of the Phayao fault zone. However, a relationship between those geometric complexities and the rupture evolution of the 2014 Thailand earthquake is still elusive, which is critical to understand complex nature of the earthquake physics and to assess the hazard. Here we elaborated the newly developed flexible finite-fault inversion method, used it to invert the globally observed teleseismic P waveforms, and estimated the spatiotemporal distribution of both the slip and the fault geometry. We found the complex rupture evolution consisting of two rupture episodes along a conjugated strike-slip fault system that comprises two distinct fault planes. The fault system derived from our finite-fault solution exhibits geometric complexities including bends, which may have caused the perturbation of the rupture propagation and the triggering of the distinct rupture episodes. Our source model of the 2014 Thailand earthquake shows that even in the case of smaller-scale earthquakes, the rupture evolution can be complex when the underlying fault geometry is multiplex.

Introduction

The seismicity of Thailand is relatively low: less than 10 earthquakes with a magnitude greater than 5 have been registered since the 1970s [1] (Fig. 1). Although situated in a low seismicity zone, Thailand is surrounded by major active faults, such as the Sagaing Fault in Myanmar and the major Aliao Shan-Red River fault north of Thailand [2] (Fig. 1). These faults are subject to a progressive clockwise strain rotation caused by the motions induced by the escape tectonics from the Tibetan Plateau to SE Asia and the Sumatra-Andaman subduction zone [2–6]. Thailand has complex geological structures that include multiple active fault zones [2,5] (Fig. 1). Many active fault zones in Thailand are part of a strike-slip fault system trending northeast-southwest and northwest-southeast [2,7]. These trends are a result of the development of the major Cenozoic rift basin that is subject to a north-south compression and east-west extension. Geological records suggest that there is historical seismicity since the Late Quaternary in the northern part of Thailand associated with the active fault zones [8,9]. One of the largest historical earthquakes in 1545 collapsed an immense pagoda in Wat Chedi Luang temple in Chiang Mai province [10] (Fig. 1).

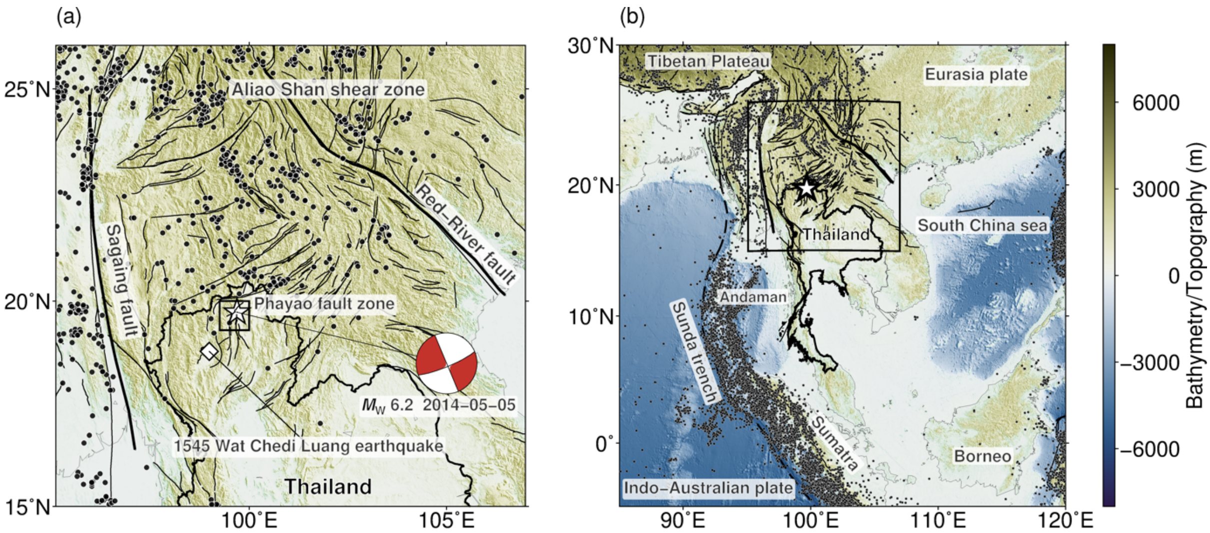

Figure 1. Seismo-tectonics summary of the study region. (a) The beach ball shows the GCMT solution of the 2014 Thailand earthquake [11]. The star is the mainshock epicentre. The dots show the seismicity between 1970 to 2014 before the mainshock from the ISC Bulletin [1]. The rectangle denotes the Phayao fault zone and the map region of Figure 2. The lines are the active faults [12]. (b) The wider view of the study region. The rectangle is the map region of Figure 1a. The dots show the seismicity between 1970 to 2014 before the mainshock from the ISC Bulletin [1]. The lines are the active faults [12]. The bathymetry/topography is from GEBCO [13]. The figures were made with Generic Mapping Tools[14].

The largest recent earthquake in Thailand, which is a focus of this study, had a moment magnitude (M_W) 6.2 and occurred in the northern part of the country on 5 May 2014 [11,15]. The 2014 Thailand earthquake affected 7 provinces, damaged more than 7000 buildings, and caused 1 death and 107 injuries [16–18], although there is a lack of direct evidence of surface rupture from satellite images [19]. The source region is situated in the Phayao Fault Zone (PFZ) [8,20], and the epicentre of the 2014 Thailand earthquake [15,21–23] is located at the transition zone within the conjugated fault system of two major active strike-slip faults; the Mae Lao Fault (MLF) trending ENE-WSW and the Phan Fault (PF) trending N-S [15,23] (Fig. 2).

A relocated hypocentre of the 2014 Thailand earthquake[15] is located at 19.733°N and 99.689°E with a 5 km hypocentral depth that is between the middle of the MLF and the top of the PF (Fig. 2). The centroid moment tensor solution shows the nodal planes orienting NNW-SSE and ENE-WSW with M_W 6.2[11]. The relocated aftershocks during the first week [15] can be divided into two major aftershock groups: the N-S trending aftershocks (NSTA) and the ENE-WSW trending aftershocks (EWTA) (Fig. 2). The regional moment tensor solutions of the aftershocks [15] are located along the NSTA and EWTA, with their strike directions aligned with the trends of the NSTA and EWTA (Fig. 2).

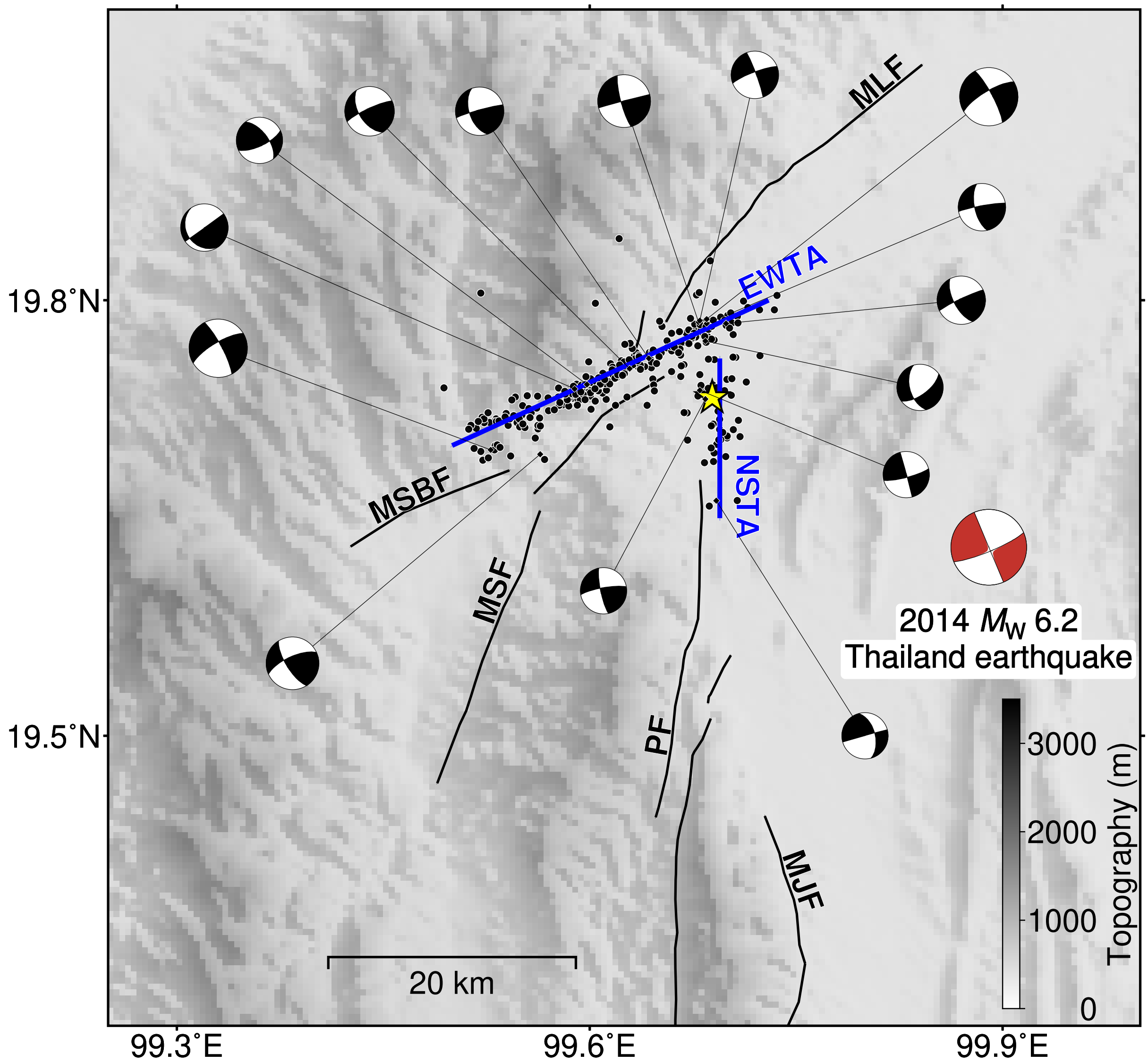

Figure 2. The study area of the 2014 Thailand earthquake. The yellow star shows the epicentre. The red beachball shows the GCMT solution of the 2014 Thailand earthquake [24,25]. The black beach balls show the focal mechanism of the relocated aftershocks with the moment magnitude larger than 4.2 [15]. The solid blue lines highlight the aftershock lineations of the NSTA and EWTA. The solid black lines are the active faults of the Phayao fault zone [26,27]: MLF; Mae Lao fault, PF; Phan fault, MSF; Mae Suai fault, MSBF; Mae Suai Boundary fault, and MJF; Mae Jai fault. The topography is from GEBCO [13]. The figure was made with Generic Mapping Tools[14].

The regional moment tensor solutions of the mainshock and the aftershocks[23] show that the principal compressive stress orientation is NNE-SSW (N18E) that is consistent with the regional stress orientation in northern Thailand [23,28,29]. The high shear stress zone is related to the strike orientation of the active MLF that is close to the EWTA: N30E-N50E. This high shear stress zone contributes to the initiation of slip based on Mohr-Coulomb failure criteria [23]. Pananont et al. [15] studied the aftershocks sequence occurring within hours by analyzing the changes in the stress field due to the rupture, for which they computed the Coulomb stress changes: they suggested that the mainshock occurred on the right-lateral faulting along the NSTA. They argued that the complex rupture process that has produced the complicated pattern of the aftershock distribution has a more elaborate geological and geomechanical origin. However, the source mechanism of the 2014 Thailand earthquake has not been clearly understood; whether the rupture evolves along the apparent conjugate fault system inferred from the aftershock distribution. The detailed imaging of the source process of the 2014 Thailand earthquake should be a critical basis to illuminate the causative relationship between the rupture evolution and the geometric complexity in the fault system for the smaller-scale, $M6$-class earthquake, which has been difficult to investigate in a means of finite-fault inversion.

A possibility of the complex fault geometry can be expected from a simple observation of the teleseismic waveforms. If an earthquake occurs along a single, simple fault plane, the teleseismic waveforms at stations within the same quadrant of the focal mechanism are expected to be similar without being contaminated by too many reflection/refraction phases. In the case of the 2014 Thailand earthquake, the stations TIP and ARU are in the same quadrant of the GCMT moment tensor solution (Fig. 3). The waveforms of the TIP and ARU stations show the different waveform shape and amplitude, which is unexpected if the earthquake rupture propagates along a single flat plane with a constant slip vector [30]. This may imply that the mainshock mechanism may involve geometric complexity. In addition, the aftershock distribution with two major trends of the NSTA and EWTA (Fig. 2) may suggest the complexity of fault geometry of the mainshock. To resolve the possible complex fault geometry, we apply a new framework of the flexible finite-fault inversion algorithm for teleseismic body waveforms [31]. We introduce a relative weight smoothness constraint that is proportional to the components of each basis moment tensor [32] into the potency density tensor inversion of Shimizu et al. [33] which can mitigate the effect of the modelling errors originating from the uncertainty of Green's function [34] as well as the uncertainty of fault geometry [35] (see details in the Method section). This method can simultaneously estimate the distribution of the focal mechanism and the slip along the assumed model plane; it enables the reconstruction of complex rupture processes, including those occurring along faults containing fault bends and those consisting of multiple subevents, without a priori assumption of the fault geometry [30,31]. The improved flexible finite-fault inversion framework has been applied to large earthquakes such as the 2020 M_W 7.7 Caribbean earthquake [30] and the 2018 M_W 7.9 Gulf of Alaska earthquake [31], but it has never been applied to smaller-scale $M6$-class earthquakes like the 2014 Thailand earthquake. In this study, we apply the flexible finite-fault method to the teleseismic body waves of the 2014 Thailand earthquake. We estimate the spatiotemporal distribution of both the slip and the fault geometry. We then discuss the detailed source process of the 2014 Thailand Earthquake, which is heavily controlled by the geometric complexity of the fault system and the associated local stress field.

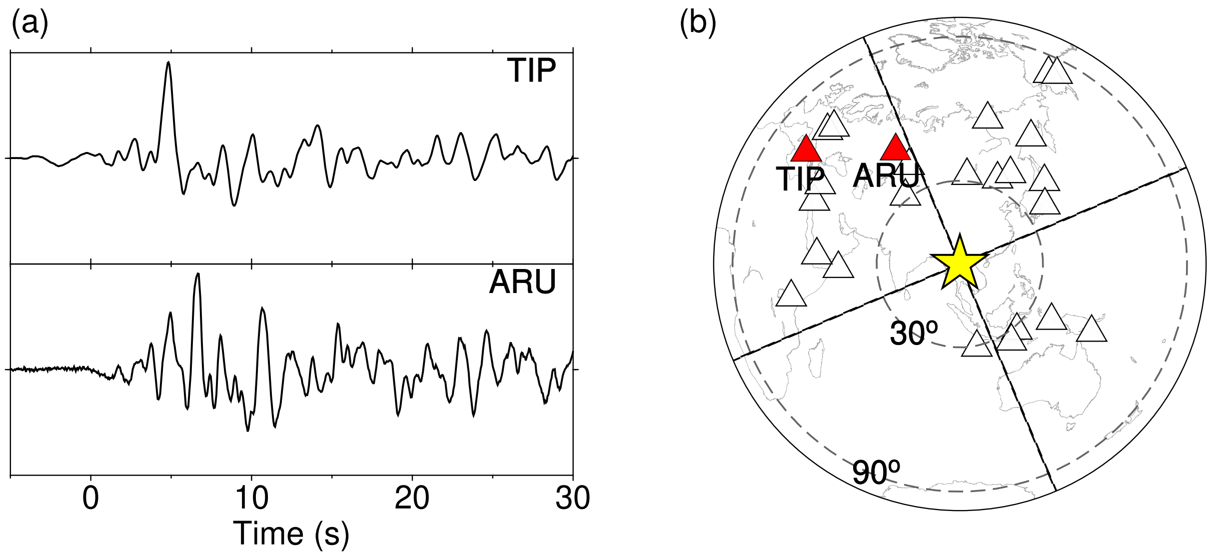

Figure 3. The station distribution and waveform examples of the 2014 Thailand earthquake. (a) The selected self-normalized waveform traces at the TIP and ARU stations. Time zero means the first arrival of the P-wave. (b) The station distribution (triangle) for the finite-fault inversion. The yellow star denotes the epicentre. The dashed lines show epicentral distances at 30° and 90°. The solid lines are the GCMT nodal direction of strikes at 67° and 337°. The figures were made with Generic Mapping Tools[14].

Method: Relative weight potency-density inversion

To construct a rupture model of the 2014 Thailand earthquake, we apply the flexible teleseismic finite-fault inversion of Shimizu et al. [33]. The method can resolve the fault geometry and the slip along the flexible assumed model plane without a priori fault geometry assumption; it represents the shear-slip vectors with five basis double-couple moment tensor components [32]. The method is based on the novel finite-fault inversion of Yagi & Fukahata [34], which can mitigate the modelling error originating from the uncertainty of Green's function. The observation equation is defined as

$$u_j(t) = \sum_{q=1}^{5} \int_S \left(G_{qj}(t,\xi) + \delta G_{qj}(t,\xi)\right) * \dot{D}_q(t,\xi) d\xi + e_{bj}(t)$$

where u_j is the teleseismic waveform at station j. G_{qj} is Green's function for the q^{th} component of the basis double-couple moment tensor at station j, and δG_{qj} is the error of Green's function. $\dot{D}_q$ is the potency-rate density function for the q^{th} component of the basis double-couple moment tensor at the source location ξ of the assumed model plane (S). e_{bj} is the background and instrument noises.

Although the method can resolve both fault geometry and slip[33,36], the source focal mechanism change within subevent is still difficult to reveal because of the spatiotemporal smoothing constraint which was introduced by the Gaussian with a same covariance into the potency-rate density function without distinguish for all five basis double-couple components. This may introduce bias because the potency-rate density of the dominant basis component becomes smoother than those of the minor components.

To mitigate the bias due to the smoothing constraints, we applied a new framework of the relative weight smoothness constraint[30,31] : it adds an inverse relative weight parameter ($1/W_q$) to the standard deviation of each basis component that is proportional to the double-couple component of the GCMT moment tensor solution (Fig. S1). To avoid the instability of the solution due to the extremely small relative standard deviation, we set the minimum weight smoothness constraint to 5% of the maximum relative standard deviation, after evaluating its sensitivity to the solution (Figs. S2 and S3; Text S1). This new framework has been proven efficient for the analyses of the source process of the 2018 Gulf of Alaska earthquake [31] and the 2020 Caribbean earthquake [30]. There it solves the problem of over-smoothing the slip distribution of the major components and allows more clear capture of the rupture propagation.

The GCMT solution [24,25] for the 2014 Thailand earthquake, shows dominant strike-slip faulting associated with the pure strike-slip M1 and M2 moment tensor components [32] (Fig. S1). Therefore, the smoothing constraint adopted in this study introduces dominant strike-slip components than for other components like the vertical slip components M3, M4 and M5 (Fig. S1).

Before applying our newly developed inversion method to the real dataset in the following sections, we first evaluate the resolvability of this approach by performing a numerical test using synthetic waveforms based on the dipping planes of conjugate faults, which are roughly akin to the hypothesised fault system of the 2014 Thailand earthquake (see Text S2). The numerical test shows that the inverted solution can well reproduce the input, which suggests that our new framework of finite-fault inversion can resolve complex ruptures even for cases of smaller-scale (*M*6-class) events consisting of multiple rupture segments and with geometric changes in the fault system.

Data and model setting

For the analysis of the 2014 Thailand earthquake rupture, we use 25 vertical components of the globally observed teleseismic waveforms (Fig. 3b) obtained from the Global Seismographic Network and the Federation of Digital Seismograph Network provided by Incorporated Research Institutions for Seismology Data Management Center. The data are selected based on signal-to-noise ratio high-enough to distinguish the *P*-wave arrival and to ensure azimuth coverage (Fig. 3) Although the earthquake magnitude is small, the waveform at the first 10 s can be distinguished from the noise level (Fig. S4). We manually pick the first arrival of *P*-wave and convert it into a velocity waveform to remove the instrument response. Then we resample it at 0.2 s. Following Kikuchi and Kanamori [32], we calculate Green's function at 0.1 s sampling rate for the components of each basis moment tensor. The finer sampling of Green's function with respect to the observed waveform sampling ensures sufficient resolution for the time shift relating to location of each subfault to the hypocentre. After this, we resample Green's function at 0.2 s, which is the waveform sampling rate. The simplified 1-D near-source structural velocity model from Wongwai et al. [37] is applied to calculate the Haskell propagation matrix for Green's function (Table S1). The sensitivity of the near-source velocity model is evaluated by testing different models (Figs. S5 and S6; Text S1), and we find our solution is not affected by the structural model. The attenuation time constant t* for the teleseismic P-waveform is about 1 s [34], and the amplitude of the signal below 1 s is very weak, so the signal is not affected by aliasing even if the sampling interval is shorter than 1 second (Fig. S7). Therefore, we do not apply a low-pass filter to both the observed waveforms and the theoretical Green's functions according to the Shimizu et al. [33] to avoid complicating the structure of the observation error by applying a low-pass filter to the observation error. The assumed model plane is confined by the relocated aftershock distribution and covers the NSTA and EWTA that are the expected rupture fault planes. The method we use allows the assumption of a horizontal model plane that is independent of the actual fault plane(s); however, such a supposition can produce a very smooth solution that will impair the interpretation of the rupturing path or the fault geometry. This problem is distinct in the conjugate strike-slip fault earthquakes with multiple fault planes because if the model space is wide and covers unnecessary space where the slip is unlikely to occur, then the unnecessary slip is squeezed out from the actual slip due to the smoothing effects. To mitigate this issue, Yamashita et al. [31] restricted the horizontal model plane only to the aftershock region, and obtained a non-rectangular plane; in that way, the rupture propagation is captured in detail and the solution is more stable [31]. We assume the model plane to have a strike of 60° and a dip of 0°. The model plane is a non-rectangular horizontal model plane with a maximum total length of 25 km along the EWTA and 12 km along the NSTA. The sub-fault has a dimension of 2×2 km^2 and lies along the strike and the dip. The moment-rate function for each sub-fault is represented as a linear B-spline function with a duration of 7.2 s. The total rupture duration is set at 9.0 s. We tested alternative assumptions of the total rupture duration (Fig. S8; Text S1) and found that 0–6 s is robustly resolved, but later period, e.g., during 6–9 s is affected by the assumption of total duration. So we here focus our discussion on the robust rupture process during 0–6 s in the following sections. The maximum rupture velocity is set at 3.6 km/s (Figs. S9 and S10; Text S1) and is approximated from the preliminary rupture duration around 7 s at a distance of 25 km from the assumed model fault plane. The approximated value is also equal to the first layer shear wave velocity (V_s) of the simplified structural velocity model [37] (Table S1). As the initial rupture point, we use the relocated hypocentre with coordinates 19.733°N, 99.689°E at 5 km depth [15].

Results

The total moment tensor solution, calculated by the integration of all potency-rate density tensors, exhibits strike-slip faulting with the two nodal planes striking at 249° (ENE-WSW) and 339° (NNW-SSE) (Fig. 4a). The moment-rate function shows at least two rupture episodes. One is between 0 and

1.5 s with a low moment-rate and the other is between 1.5 and 4.5 s with a high moment-rate. The highest moment-rate occurs at around 3.5 s (Fig. 4b). The total seismic moment is 0.36×10^{19} Nm (M_W 6.3), which is slightly larger than the GCMT solution (M_W 6.2) and the USGS W-phase moment tensor (M_W 6.1). The larger seismic moment in our work is probably due to our model covering a wider area that includes the aftershock distribution along the NSTA and EWTA.

The static distribution of the potency density reveals two large potency zones located in the middle of the EWTA and one in the middle of the NSTA. The larger potency density in the EWTA is around 1.8 m and the potency density in the NSTA is around 1.3 m (Fig. 4c). The nodal plane distribution of the potency density shows that the strike orientation rotates clockwise along the EWTA from 240° to 265° (Fig. 4c) and along the NSTA from 7° to 24° (Fig. 4c).

The spatiotemporal distribution of the potency-rate density exhibits two rupture episodes, one along the NSTA and the other along the EWTA (Fig. 5a). The initial rupture of the mainshock originates at the hypocentre in the first 1.5 s and propagates south along the NSTA at a rupture speed of ~3.0 km/s. The second rupture occurs at the eastern edge of the EWTA between 1.0 s and 1.5 s and propagates southwest along the EWTA at a rupture speed of ~3.5 km/s (Fig. 5a). The second rupture has the highest potency-rate in the middle of the EWTA between 2.0 and 3.0 s and terminates at the west end of the EWTA at 4.5 s. These two rupture episodes coincide with the dominant peaks seen in the moment-rate function (Fig. 4). The spatiotemporal distribution of the moment tensor solution shows two dominant patterns of strike-slip faulting, both with smaller-scale fluctuation of the fault geometry in each lineation (Fig. 5b). One with a strike at NNE-SSW near the epicentre occurred between 0.5 and 1.5 s and the other with a strike at ENE-WSW northwest from the epicentre occurred between 1.5 and 4.0 s. The nodal plane distribution extracted from the resultant spatiotemporal potency-rate density tensor (Fig. 5b) exhibits clockwise strike rotation from ~18° to ~33°. For the rupture propagating from the epicentre towards the south along the NSTA during the first 1.5 s, this rotation coincides with the timing when the large potency-rate density is observed. The clockwise rotation of the strike also occurs from the middle to the west end of the EWTA from ~218° to ~250°; it is associated with the second rupture arising at the eastern edge of the EWTA, propagating west during the period between the 2.0 and 3.5 s and having the highest potency-rate of around 1.2 m/s (Fig. 5b). These spatiotemporal changes of fault geometry are robust for different assumptions of the regional structural velocity model and of the maximum rupture velocities (Figs. S5 and S6; S9 and S10).

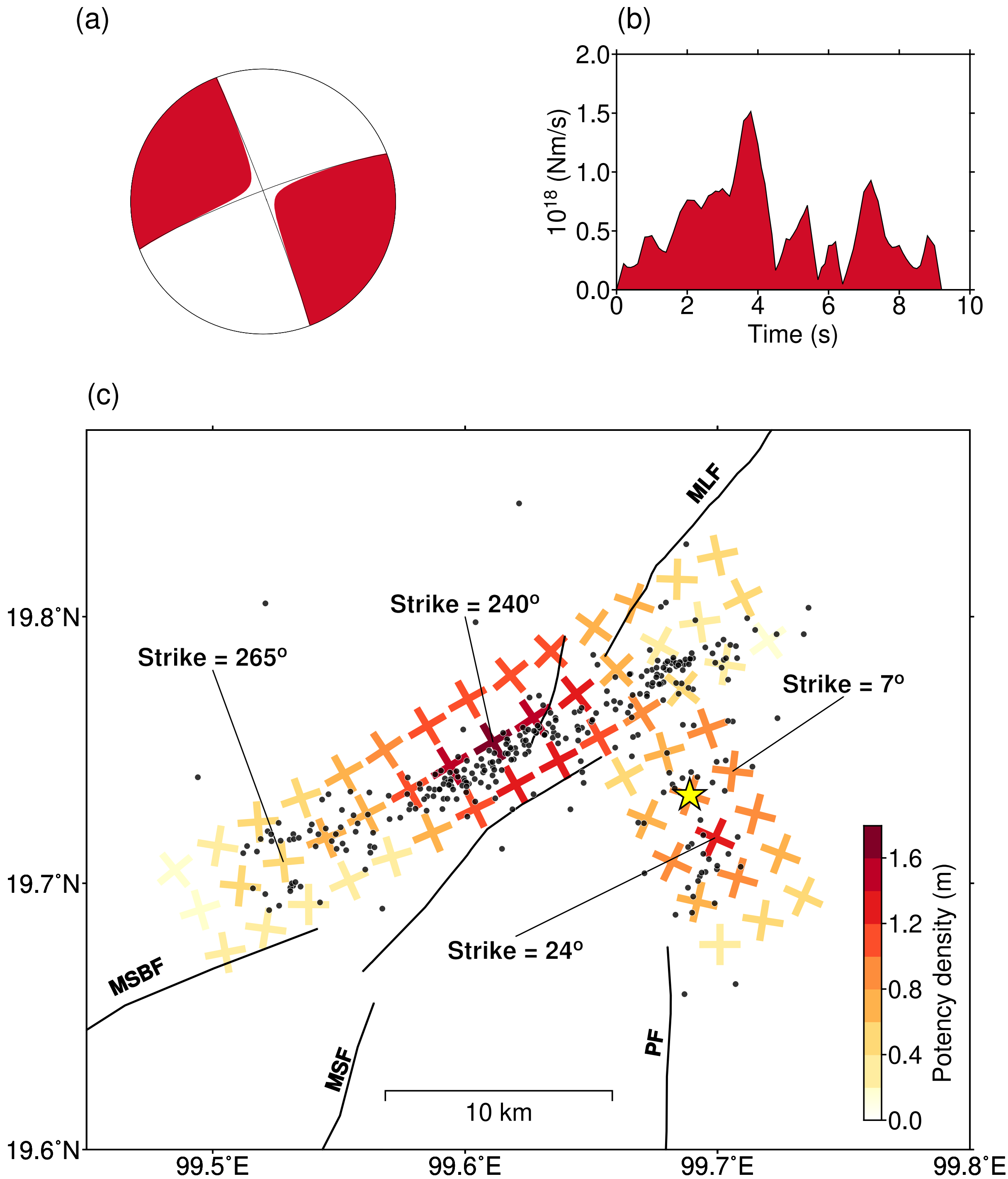

Figure 4. The summary of the result. (a) The total moment tensor solution. (b) The moment-rate function. (c) The distribution of the potency density and strike orientation extracted from the potency density tensor of each sub-fault along the assumed horizontal model plane. The crossmark represents the strike orientation of the nodal planes and its color shows the amount of potency density. The yellow star denotes the epicentre. The dots are the relocated aftershocks [15]. The black solid lines are the active faults [26,27]: MLF: Mae Lao fault, PF; Phan fault, MSF; Mae Suai fault, MSBF; Mae Suai Boundary fault. The figure was made with Generic Mapping Tools[14].

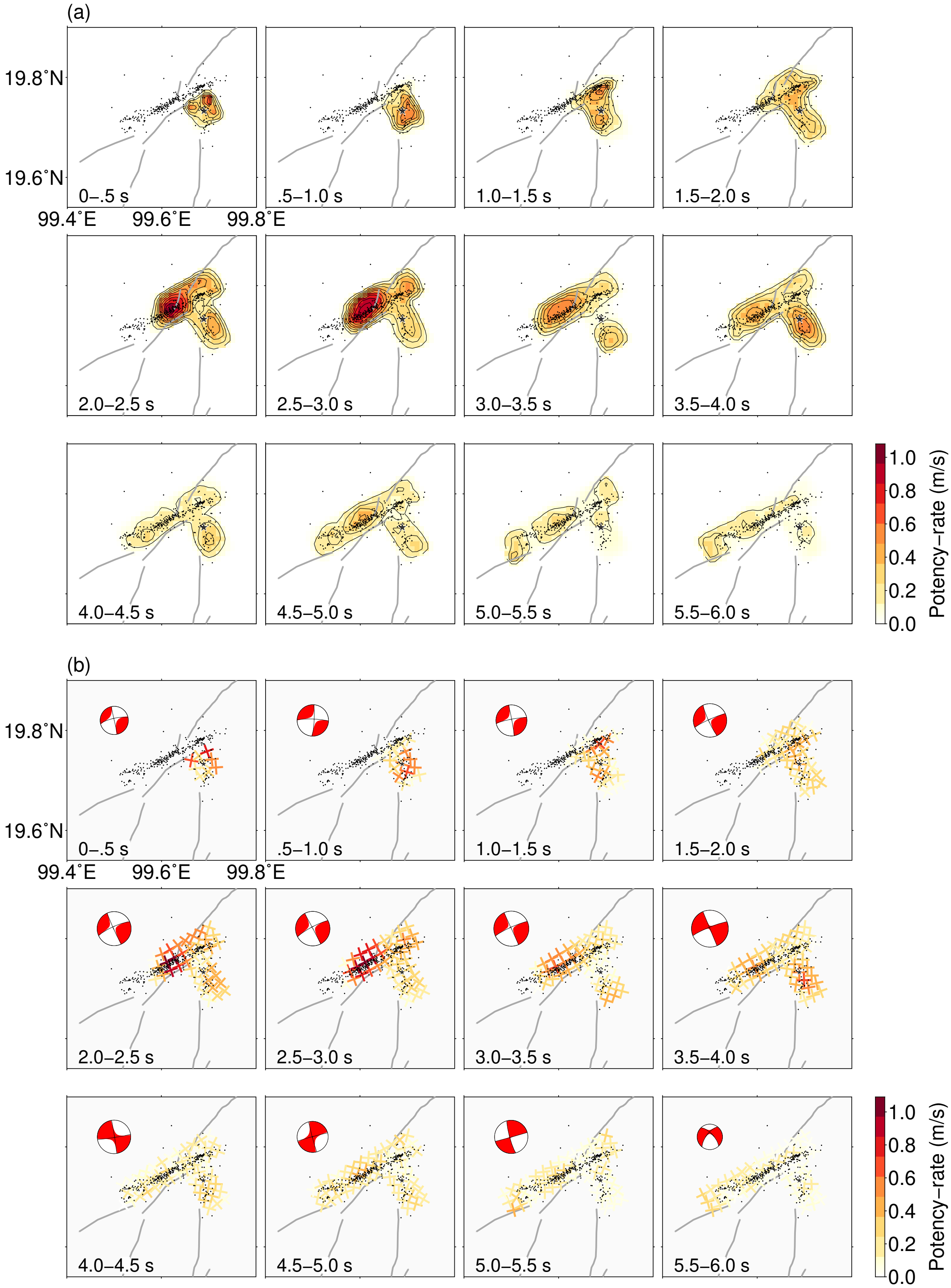

Figure 5. The spatiotemporal distribution of the potency-rate density. (a) The panels show the contour plot of the potency-rate density distribution. (b) the panels show the nodal planes distribution extracted from the potency-rate density tensor. The corresponding time window of (a) and (b) is presented as the averaged snapshot of the potency-rate density tensor. The beach ball shows the total moment tensor solution within the time window. The star shows the epicentre. The dots show the relocated aftershock [15]. The line shows the active faults [26,27]. The figures were made with Generic Mapping Tools[14].

Discussion

Our finite-fault source model of the 2014 Thailand earthquake distinguished two rupture episodes that show a dominant strike-slip faulting consisting of different rupture lineations along the NSTA and EWTA (Fig. 5), which are consistent with the nodal plane distribution (Fig. 4c) and thus facilitates identification of the possible fault geometry for the 2014 Thailand earthquake. The nodal plane distribution along the NSTA shows nodal strikes in the NNE-SSW direction and the auxiliary plane in the ESE-WNW direction (Fig. 4). The nodal plane distribution along the EWTA shows nodal strikes in the ENE-WSW direction and the auxiliary plane in the NNW-SSE direction (Fig. 4). The consistency between the nodal plane distribution (Fig. 4c) and the rupture directions of the spatiotemporal potency-rate density distribution (Fig. 5) facilitates identification of the possible fault geometry. The striking plane along the NSTA is determined to be in the NNE-SSW direction and is associated with the rupture propagating towards the south. The striking plane along the EWTA is determined to be in the ENE-WSW direction and is associated with the rupture propagating towards the southwest. The obtained two dominant fault planes along the NSTA and EWTA are consistent with the two distinct trends of the relocated aftershock distribution [15]. The first is the N-S trend (~180° from north) along the NSTA located near the epicentre and the second is the ENE-WSW trend (~60° from north) along the EWTA located northwest from the epicentre. Although the geometry of our model, designed to cover the aftershock distribution area, is non-rectangular, the potency density and the potency-rate density of each sub-fault are estimated independently from the assumed model geometry.

The strike orientation of the potency density tensor shows geometric bends; since they are changes in the strike direction of the rupture-hosting fault, they play an important role in the earthquake rupture process [38,39]. Our finite-fault model shows that the lineations of the strike directions in the NSTA (7° to 24° of the reference points in Fig. 4) and EWTA (240° to 265° of the reference points in Fig. 4) coincide with the spatial pattern of the aftershock distribution. In addition to these general lineations of the fault geometry, the strike orientation of the spatiotemporal potency-rate density tensor distribution (Fig. 5b) also shows dynamic changes of the fault geometry. During the first 1.5 s, the strike orientation rotates clockwise as it propagates from the northern to the southern edges of the NSTA (Fig. 5b). Then, at around 1.5 s as the rupture migrates from the NSTA to the EWTA, the fault strike direction changes from NNE-SSW at the northern edge of the NSTA to ENE-WSW at the eastern edge of the EWTA, which implies that the fault planes in the NSTA and EWTA can be considered as a conjugate fault, where the planes inclined at angles on either side of the maximum principal stress [40]. Next, between 2.0 and 3.5 s the second rupture propagates along EWTA from its eastern edge towards the south-west and terminates at around 4.5 s at its western edge. In this process, the time at which the strike orientation rotates clockwise corresponds to the time of the largest potency-rate density. It is associated with the second rupture arising at the eastern edge of the EWTA, propagating west during the period between the 2.0 and 3.5 s and having the highest potency-rate of around 1.2 m/s (Fig. 5b). Our result of the major slip along the EWTA during 2–3 s is robustly resolved even if we change the assumptions of maximum rupture velocity, the total durations (Figs. S8 and S10). According to the surface fault lines [23,26], the orientation of the known active conjugated strike-slip faults of the PF and MLF shows striking at N5E–N13E and N30E–N50E; this is consistent with our findings that at the northern edge of the NSTA, the striking is in the NNE-SSW direction and at the eastern edge of the EWTA, in the ENE–WSW direction. The multiple sub-events at the conjugated strike-slip fault system are possibly due to the complex rupture evolution [31,41]. Therefore, we conclude that the rupture evolution of the 2014 Thailand earthquake is characterized by multiple sub-events in the conjugated strike-slip fault system of the PF and MLF. We here echo that we observed the largest potency-rate density tensor distribution at 2.0–2.5 s. Then, at 3.5–4.5 s, the potency-rate density reduces after the bend, where we see the change of strike angles from ~218° to ~250° (Fig. 5b). Furthermore, studies using the flexible teleseismic finite-fault inversion have shown that complexities in the faulting system, like geometric bends, can cause the non-smooth rupture propagation of the mainshock [30,31,42]. The dynamic rupture simulation demonstrates that rupture perturbation could have occurred from the bend along a strike-slip faulting [38,43]. Thus, we suggest that the rupture along the NSTA and EWTA exhibits the complexity of the fault geometry that includes a bend. This complicated fault system is the reason for the fluctuation of the rupture front. It also can act as a barrier for the termination of the rupture propagation at the southern edge of the NSTA and the western edge of the EWTA. The possible bends of the fault system can also be seen in the relocated aftershock distribution in the south of the epicentre and the western edge of the EWTA (Fig. 4), which may contribute to confine the rupture along NSTA and facilitates the major rupture along the EWTA.

The rupture evolution of the 2014 Thailand earthquake displays two distinct rupture episodes with rupture directions along the NSTA and EWTA. These rupture episodes reveal two perpendicular planes that coincide with the aftershock distribution pattern along the NSTA and EWTA (Fig. 5). The aftershock distribution shows a spatial gap of around 5 km located between the northern edge of the NSTA and the eastern edge of the EWTA (Figs. 4 and 5). In this gap, our source model shows the lowest potency-rate density for the entire rupture duration between the northern edge of the NSTA and the eastern edge of the EWTA (Fig. 5). The agreement between the low potency-rate density area and the spatial gap in the aftershock distribution suggests that the two conjugate faults are not connected. The discontinuity of the co-seismic slip across the gap in the conjugated fault system suggests that the second rupture episode initiated at the eastern edge of the EWTA may have been triggered by the initial rupture episode along the NSTA.

The spatial distribution of the P-axis (or the maximum compressive stress axis) azimuth, extracted from the potency density tensor for each sub-fault (Fig. 6) exhibits clockwise rotation from the northern edge to the southern edge of the NSTA, from 52° to 69° azimuths, and from the eastern edge to the western edge of the EWTA, from 15° to 39° azimuth. This clockwise rotation of the P-axis azimuth is in accordance with the aftershock lineation along the NSTA and EWTA (Fig. 6a). The histogram of the P-axis azimuth distribution displays two peaks, one at 10°–30° and the other at 50°–70° (Fig. 6b). Since most of the aftershocks of magnitude 4 and above, for which a focal mechanism solution is estimated by Noisagool et al. [23], occur in the EWTA [15], the principal compressive stress axis orientation of 18° obtained from the mainshock and the aftershocks of the 2014 Thailand earthquake [23] is most likely reflecting the one in the EWTA domain, which coincides with our estimates of the P-axis azimuth distribution along the EWTA (Fig. 6). Whilst, the direction of the P-axis azimuth along the NSTA obtained in this study (~50°, Fig. 6) is rotated clockwise by about 30° from the principal compressive stress axis orientation obtained by Noisagool et al., [23]. As a result, the strike-slip direction with strike of 24° at the southern part of the NSTA obtained from this study (Fig. 4), is opposite to that expected from the principal compressive stress axis orientation of 18° obtained by Noisagool et al., [23]. On the other hand, if Coulomb's friction factor is a typical value of 0.6, the two peaks of our P-axis histogram (Fig. 6) can be naturally explained as a shift of the P-axis of the conjugate fault plane [44], which leads to ~35° principal stress axis; about 15° clockwise from the principal stress axis orientation obtained in Noisagool et al. [23]. We should mention, however, the focal mechanism solutions obtained in this study are affected by dynamic changes in the stress field due to seismic waves or localized fault structures, and estimation of the principal stress axis is beyond the scope of this study. Our results suggest that further investigation of the stress field in this region is needed, taking into account the spatial bias of aftershock distribution, which affects the estimates of the principal stresses for the conjugate fault earthquake.

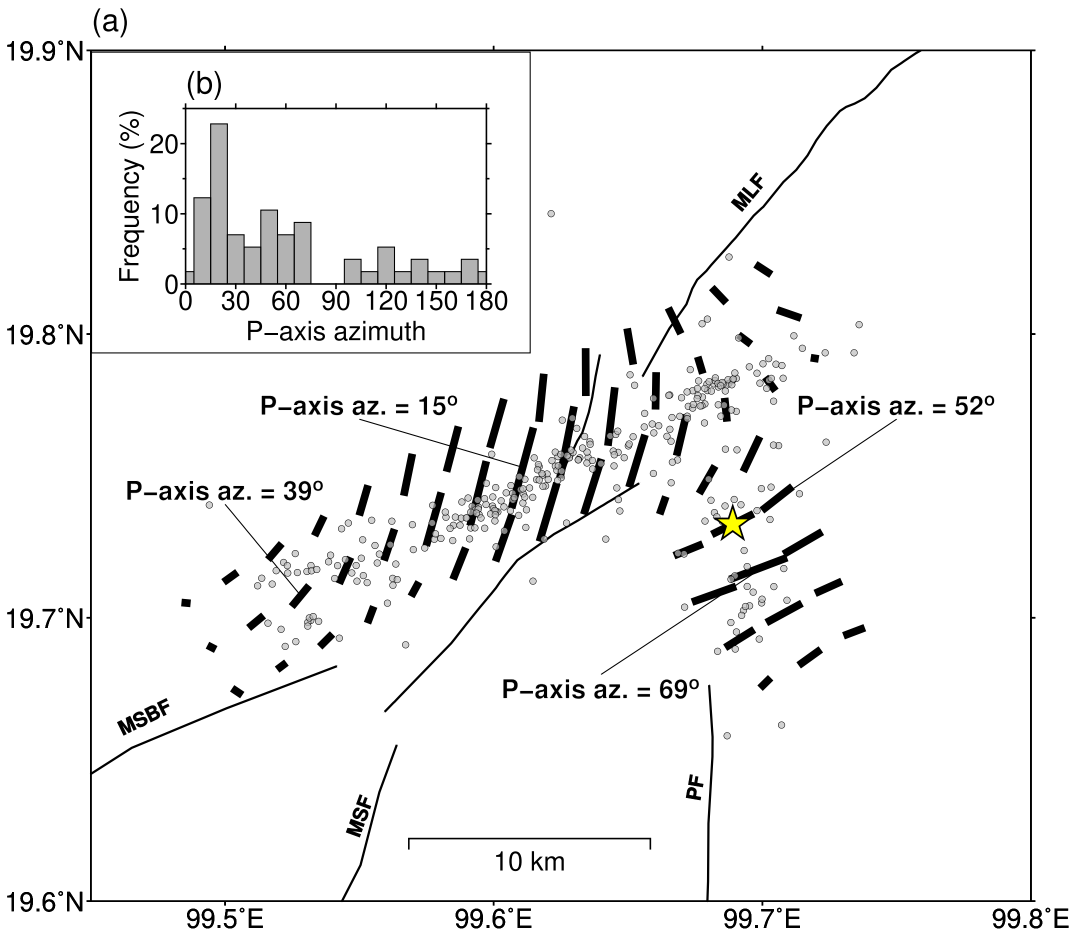

Figure 6. The P-axis azimuth distribution. (a) The P-axis azimuth distribution extracted from the resultant potency-density tensors of each sub-fault from Figure 4. The length of the P-axis is proportional to the potency density relating to the color scale of Figure 4. The azimuth is measured clockwise from north. The yellow star shows the epicentre. The dots show the relocated aftershock [15]. The black thin line shows the active faults [26,27]. (b) The histogram of the P-axis azimuth distribution with 10° azimuthal bin width, which plots between the azimuth angle and the percentage of the count of the P-axis azimuth along the model plane. The figure was made with Generic Mapping Tools[14].

Conclusion

We construct a source model for the 2014 Thailand M_W 6.2 earthquake that occurred within the Phayao fault zone in northern Thailand, by applying a new framework of the flexible teleseismic *P* waveform finite-fault inversion and resolved both the fault geometry and the slip. Our source model exhibits complex rupture evolution consisting of two rupture episodes along a conjugated strike-slip fault system that comprises two distinct fault planes. These planes coincide with the relocated aftershock distribution. The initial rupture originates at the hypocentre and propagates southward along the north-south oriented fault plane near the epicentre. Then the second rupture episode is triggered north of the epicentre at the eastern edge of the conjugated east-west oriented fault plane and propagates southwestward until the rupture terminates. Our source model shows not only the conjugate fault geometry but also the fault bends that are related to the smaller-scale features of the aftershock lineation in each rupture episode. Our model also suggests that the conjugate fault system of the 2014 Thailand earthquake is not connected at the junction; the observed spatial gap (~5 km) may account for the triggering of the second rupture episode. The spatial variation of the principal stress axis inferred from our finite-fault model suggests an in-situ stress state of the Phayao fault zone, which is responsible for the complex rupture evolution of the 2014 Thailand earthquake.

References

1. ISC. International Seismological Centre. (2021). doi:https://doi.org/10.31905/D808B830
2. Morley, C. K., Charusiri, P. & Watkinson, I. M. Structural geology of Thailand during the Cenozoic. *Geol. Thail.* 273–334 (2011). doi:10.1144/goth.11
3. Huchon, P., Le Pichon, X. & Rangin, C. Indochina Peninsula and the collision of India and Eurasia. *Geology* **22**, 27–30 (1994).
4. Leloup, P. H. *et al.* New constraints on the structure, thermochronology, and timing of the Ailao Shan-Red River shear zone, SE Asia. *J. Geophys. Res.* **106**, 6683–6732 (2001).
5. Morley, C. K. A tectonic model for the Tertiary evolution of strike-slip faults and rift basins in SE Asia. *Tectonophysics* **347**, 189–215 (2002).
6. Morley, C. K. Variations in Late Cenozoic-Recent strike-slip and oblique-extensional geometries, within Indochina: The influence of pre-existing fabrics. *J. Struct. Geol.* **29**, 36–58 (2007).
7. Charusiri, P. & Pum-Im, S. Cenozoic Tectonic Evolution of Major Sedimentary Basins in Central, Northern, and the Gulf of Thailand. *Best* **2**, 40–62 (2009).
8. Fenton, C. H., Charusiri, P. & Wood, S. H. Recent paleoseismic investigations in Northern and Western Thailand. *Ann. Geophys.* **46**, 957–982 (2003).
9. Pailoplee, S. & Charusiri, P. Seismic hazards in Thailand: A compilation and updated probabilistic analysis 4. Seismology. *Earth, Planets Sp.* **68**, (2016).
10. Kázmér, M., Sanittham, K., Charusiri, P. & Pailoplee, S. Archaeoseismology of the AD 1545 Earthquake in Chiang Mai Thailand. *2nd INQUA-IGCP-567 Int. Work. Act. Tectonics, Earthq. Geol. Archaeol. Eng. Corinth, Greece* 1–4 (2011).
11. GCMT. Mw 6.2 Chiang Rai, Thailand. (2014). Available at: https://ds.iris.edu/spud/momenttensor/9687293.
12. Styron, R. & Pagani, M. The GEM Global Active Faults Database. *Earthq. Spectra* **36**, 160–180 (2020).
13. GEBCO. Gridded Bathymetry Data Download. (2020). Available at: https://download.gebco.net.
14. Wessel, P., Smith, W. H. F., Scharroo, R., Luis, J. & Wobbe, F. Generic Mapping Tools: Improved Version Released. *Eos, Trans. Am. Geophys. Union* **94**, 409–410 (2013).
15. Pananont, P. *et al.* Seismotectonics of the 2014 Chiang Rai, Thailand, earthquake sequence. *J. Geophys. Res. Solid Earth* **122**, 6367–6388 (2017).
16. Lhamphoonsup, K., Soisa, T. & Sriwangpon, P. *PRELIMINARY GEOPHYSICAL INVESTIGATION IN AN EARTHQUAKE IMPACT AREA CHIANG RAI PROVINCE*. *Annual Meeting Report of The 2014 Chiang Rai Earthquake* (2014).
17. Wechbunthung, B. *SEISMIC DATA OF EARTHQUAKE AT CHIANGRAI ON MAY 5, 2014*.

Annual Meeting Report of The 2014 Chiang Rai Earthquake (2014).

18. Wiwegwin, W. & Kosuwan, S. *Annual Meeting Report of The 2014 Chiang Rai Earthquake*. (2014).
19. Nardkulpat, A., Phodee, P., Karnchanasuthum, S., Nualchawee, K. & Rakwatin, P. Using Differential InSAR Technique for Coseismic Displacement Study of Mw6.3 Chiang Rai Earthquake, Thailand. in *Conference: GEOINFOTECH2017* (2017).
20. Pailoplee, S., Sugiya, Y. & Charusiri, P. Determini s tic and probabili s tic s ei s mic hazard analy s e s in Thailand and adjacent area s u s ing active fault data. **61**, 1313–1325 (2009).
21. USGS. M6.1 - 13 km NNW of Phan, Thailand. (2014). Available at: https://earthquake.usgs.gov/earthquakes/eventpage/usb000qack/executive.
22. TMD Thai Meteorological Department. Mw 6.3 Chiang Rai, Thailand. (2014). Available at: https://earthquake.tmd.go.th/inside-info.html?earthquake=2085.
23. Noisagool, S., Boonchaisuk, S., Pornsopin, P. & Siripunvaraporn, W. The regional moment tensor of the 5 May 2014 Chiang Rai earthquake (Mw = 6.5), Northern Thailand, with its aftershocks and its implication to the stress and the instability of the Phayao Fault Zone. *J. Asian Earth Sci.* **127**, 231–245 (2016).
24. Dziewonski, A. M., Chou, T. A. & Woodhouse, J. H. Determination of earthquake source parameters from waveform data for studies of global and regional seismicity. *J. Geophys. Res.* **86**, 2825–2852 (1981).
25. Ekström, G., Nettles, M. & Dziewoński, A. M. The global CMT project 2004-2010: Centroid-moment tensors for 13,017 earthquakes. *Phys. Earth Planet. Inter.* **200–201**, 1–9 (2012).
26. DMR Department of Mineral Resources. Active Fault Map of Thailand. (2016). Available at: http://www.dmr.go.th/n_more_news_en.php?nid=109490.
27. Kanthiya, S., Mangkhemthong, N. & Morley, C. K. Structural interpretation of Mae Suai Basin, Chiang Rai Province, based on gravity data analysis and modelling. *Heliyon* **5**, e01232 (2019).
28. Heidbach, O., Rajabi, M., Reiter, K., Ziegler, M. & WSM Team. World Stress Map Database Release 2016. V. 1.1. (2016). doi:https://doi.org/10.5880/WSM.2016.001
29. Simons, W. J. F. *et al.* A decade of GPS in Southeast Asia: Resolving Sundaland motion and boundaries. *J. Geophys. Res. Solid Earth* **112**, 1–20 (2007).
30. Tadapansawut, T., Okuwaki, R., Yagi, Y. & Yamashita, S. Rupture Process of the 2020 Caribbean Earthquake Along the Oriente Transform Fault, Involving Supershear Rupture and Geometric Complexity of Fault. *Geophys. Res. Lett.* **48**, 1–19 (2021).
31. Yamashita, S. *et al.* Consecutive ruptures on a complex conjugate fault system during the 2018 Gulf of Alaska earthquake. *Sci. Rep.* **11**, 1–9 (2021).
32. Kikuchi, M. & Kanamori, H. Inversion of Complex Body Waves-III. *Bull. Seismol. Soc. Am.* **81**, 2335–2350 (1991).

33. Shimizu, K., Yagi, Y., Okuwaki, R. & Fukahata, Y. Development of an inversion method to extract information on fault geometry from teleseismic data. *Geophys. J. Int.* **220**, 1055–1065 (2020).

34. Yagi, Y. & Fukahata, Y. Introduction of uncertainty of Green's function into waveform inversion for seismic source processes. *Geophys. J. Int.* **186**, 711–720 (2011).

35. Ragon, T., Sladen, A. & Simons, M. Accounting for uncertain fault geometry in earthquake source inversions - I: Theory and simplified application. *Geophys. J. Int.* **214**, 1174–1190 (2018).

36. Shimizu, K., Yagi, Y., Okuwaki, R. & Fukahata, Y. Construction of fault geometry by finite-fault inversion of teleseismic data. *Geophys. J. Int.* **224**, 1003–1014 (2021).

37. Wongwai, W., Pananont, P. & Pornsopin, P. Teleseismic Receiver Functions Study of the Crustal Thickness Underneath Thailand. *Am. Geophys. Union, Fall Meet. 2013, Abstr. id. S33F-03* (2013).

38. Kase, Y. & Day, S. M. Spontaneous rupture processes on a bending fault. *Geophys. Res. Lett.* **33**, 1–4 (2006).

39. Ulrich, T. *et al.* Coupled, Physics-Based Modeling Reveals Earthquake Displacements are Critical to the 2018 Palu, Sulawesi Tsunami. *Pure Appl. Geophys.* **176**, 4069–4109 (2019).

40. Scholz, C. H. *The Mechanics of Earthquakes and Faulting*. (Cambridge University Press, 2002). doi:10.1017/CBO9780511818516

41. Meng, L. *et al.* Earthquake in a maze: Compressional rupture branching during the 2012 Mw 8.6 Sumatra earthquake. *Science (80-.).* **337**, 724–726 (2012).

42. Okuwaki, R., Hirano, S., Yagi, Y. & Shimizu, K. Inchworm-like source evolution through a geometrically complex fault fueled persistent supershear rupture during the 2018 Palu Indonesia earthquake. *Earth Planet. Sci. Lett.* **547**, 116449 (2020).

43. Duan, B. & Oglesby, D. D. Multicycle dynamics of nonplanar strike-slip faults. *J. Geophys. Res.* **110**, 1–16 (2005).

44. Iio, Y. Frictional coefficient on faults in a seismogenic region inferred from earthquake mechanism solutions. *J. Geophys. Res. Solid Earth* **102**, 5403–5412 (1997).

45. Hunter, J. D. Matplotlib: A 2D Graphics Environment. *Comput. Sci. Eng.* **9**, 90–95 (2007).

46. Beyreuther, M. *et al.* ObsPy: A Python Toolbox for Seismology. *Seismol. Res. Lett.* **81**, 530–533 (2010).

47. Laske, G., Masters, G., Ma, Z. & Pasyanos, M. Update on CRUST1.0 -A 1-degree Global Model of Earth's Crust, Geophys. Res. Abstract. in *Abstract EGU2013* 2658 (2013).

Acknowledgements

This work has been supported by a Grant-in-Aid for Scientific Research (C) 19K04030. We thank Passakorn Pananont and others for making available their relocated aftershock data and the near-source structural velocity model. We thank the Department of Mineral Resources of Thailand and the Thai Meteorological Department for making available their regional fault surface lines of the Phayao fault zone. The facilities of IRIS Data Services and specifically the IRIS Data Management Center were used to access the waveforms, related metadata, and derived products used in this study. IRIS Data Services are funded through a Seismological Facilities for the Advancement of Geoscience (SAGE) Award from the National Science Foundation under Cooperative Support Agreement EAR-1851048. The figures were generated with Generic Mapping Tools version 5 [14], Matplotlib version 3.1.1 [45], and ObsPy version 1.1.0 [46].

Data Availability

Teleseismic waveforms were obtained from the following networks: the Global Seismograph Network (GSN IRIS/IDA, II; https://doi.org/10.7914/SN/II); the Global Seismograph Network (GSN IRIS/USGS, IU; https://doi.org/10.7914/SN/IU); New China Digital Seismograph Network (NCDSN, IC; https://doi.org/10.7914/SN/IC); the Alaska Regional Network (AK; https://doi.org/10.7914/SN/AK); the Australian National Seismograph Network (ANSN, AU; http://www.fdsn.org/networks/detail/AU/); the China National Seismic Network, the Data Management Centre of the China National Seismic Network at the Institute of Geophysics (SeisDmc CEA, CB; https://doi.org/10.7914/SN/CB); the Czech Regional Seismic Network (CZ; https://doi.org/10.7914/SN/CZ); GEOFON (GE; https://doi.org/10.14470/TR560404); the Japan Meteorological Agency Seismic Network (JP; http://www.fdsn.org/networks/detail/JP/); the Kyrgyz Seismic Telemetry Network (KNET, KN; https://doi.org/10.7914/SN/KN); the Mediterranean Very Broadband Seismographic Network (MedNet, MN; https://doi.org/10.13127/SD/fBBBtDtd6q); and the Austrian Seismic Network (OE; https://doi.org/10.7914/SN/OE). The moment tensor solutions were obtained from the GCMT catalog (https://www.globalcmt.org/CMTsearch.html). The CRUST 1.0 structural velocity model of Laske et al. [47] is available at https:// igppweb.ucsd.edu/~gabi/crust1.html. The topography and bathymetry data from GEBCO are available at https://download.gebco.net. The global database of the major active faults from Styron and Pagani [12] is available at https://github.com/GEMScienceTools/gem-global-active-faults.